

Modeling Weakly Scattering Random Media: A Tool to Resolve the Internal Structure of Nanoporous Materials

Alberto Jiménez-Solano, José María Miranda-Muñoz, Sol Carretero-Palacios,*
and Hernán Míguez*

Nanoporous media scatter a small fraction of the light propagating through them, even if pore sizes are significantly smaller than the characteristic visible wavelengths. The disordered spatial modulation of the refractive index at the few or few tens of nanometers length scale, resulting from the presence of randomly distributed air bubbles or solid aggregates within a continuous solid background, gives rise to these weak scattering effects. However, standard theoretical approaches to describe this kind of media use effective medium approximations that do not account for diffuse, ballistic, and specular components. Herein, all spectral components and the angular distribution of the scattered light are captured through optical modeling. A Monte Carlo approach, combining scattering Mie theory and Fresnel equations, implemented within a genetic algorithm, allows us to decode the void and aggregate size distribution and hence the internal structure of a nanocrystalline titania (TiO₂) film chosen as a paradigmatic example. The approach allows to generically describe the scattering properties of nanoporous materials which, as shown herein, may be used to decipher their internal structure from the fitting of their far-optical field properties.

optics,^[2] biomedical optics,^[3] structural color,^[4,5] or astrophysics,^[6] among others. Recently, findings in transport properties of classical light in complex media have been extended to the quantum realm,^[7] demonstrating that quantum properties of light can also be controlled while traversing a complex scattering medium. In material science, propagation of light through complex media has been extensively discussed in correlated disordered media as well.^[8] Many porous natural and man-made materials can be considered as optically disordered media, that is, materials in which the refractive index varies spatially in a random way in distances comparable to the characteristic wavelengths of the optical regime. Their interaction with light gives rise to diffuse scattering, which is in fact their most reckonable optical feature. Ceramics, rocks, sea foams, or biological tissues are examples of such light-diffusing systems, the latter


1. Introduction

Light transport in disordered media is a fascinating and mature topic discussed in the framework of imaging,^[1] atmospheric

being the subject of intense research on the grounds of inverse design, for instance, using the inverse adding–doubling^[9] technique to retrieve their optical properties. Weakly scattering materials typically display a nanoporous internal structure that is typically characterized by a large specific surface area^[10] with potential technological applications, relevant to a wide number of fields and industries, including chemical synthesis,^[11,12] energy,^[13–15] catalysis,^[16] drug delivery,^[17] photonics,^[18,19] or sensing.^[20] Also, scattering by nanoporous structures has recently been shown to be relevant to either analyze^[21] or determine^[22] fundamental physical phenomena occurring at the nanoscale.

To a great extent, the properties of nanoporous materials depend on their overall porosity and pore size distribution, the former being key to developing applications for energy generation and storage systems, membranes, or catalysts. For instance, they will affect the material optical response, as pores may adsorb vapors present in the environment as a function of their partial pressure, modifying its effective refractive index.^[23] Optical properties of weakly scattering porous materials are commonly theoretically described through homogenization theories, in which the macroscopic properties of a complex electromagnetic composite are described as if it was a homogeneous effective medium. The most commonly employed effective medium approximation models are Bruggeman^[24] and

A. Jiménez-Solano
Departamento de Física
Universidad de Córdoba
Edificio Einstein (C2), Campus de Rabanales, 14071 Córdoba, Spain
J. M. Miranda-Muñoz, H. Míguez
Instituto de Ciencia de Materiales de Sevilla
Consejo Superior de Investigaciones Científicas – Universidad de Sevilla
(CSIC-US)
Américo Vespucio 49, 4109 Seville, Spain
E-mail: h.miguez@csic.es
S. Carretero-Palacios
Departamento de Física de Materiales and Instituto Nicolás Cabrera
Universidad Autónoma de Madrid
Campus de Cantoblanco, 28049 Madrid, Spain
E-mail: sol.carretero@uam.es

 The ORCID identification number(s) for the author(s) of this article can be found under <https://doi.org/10.1002/adpr.202200267>.

© 2023 The Authors. Advanced Photonics Research published by Wiley-VCH GmbH. This is an open access article under the terms of the Creative Commons Attribution License, which permits use, distribution and reproduction in any medium, provided the original work is properly cited.

DOI: 10.1002/adpr.202200267

Maxwell–Garnett^[25] theories, which provide the permittivity of the effective medium in terms of the permittivities and volume fractions of the individual constituents of the complex medium. Using those models combined with a standard transfer-matrix method (TMM),^[26] optical properties such as ballistic transmittance and specular reflectance can be computed. However, light impinging normally onto porous materials can either go through them keeping the initial illumination direction, yielding ballistic transmission and specular reflection, or be deviated from the straight direction, contributing to diffuse scattering. The probability of each one of these phenomena to occur, as well as the angular distribution of the diffusely scattered light, cannot be modeled with the abovementioned standard approaches.

Here we present a theoretical method to optically characterize weakly scattering optical media, which allow distinguishing amongst ballistic, specular, and scattered light components. Results also provide the angular distribution of diffusely scattered light. We select as illustrative example a TiO₂ porous matrix of 50% porosity,^[27] relevant for a wide range of technological applications, such as photocatalysis and photovoltaics.^[4,5,28,29] The mesoporous TiO₂ film is modeled as a mainly nonscattering homogeneous TiO₂ film of 50% porosity, described as an effective medium inside which a dilute concentration of TiO₂ and air aggregates is randomly distributed. These are responsible for the weak light scattering effect observed, which is the main target of our research work. In our approximation, these aggregates are represented as a nonorderly, nonmonodispersed, distribution of spherical nanoparticles, made up of TiO₂ and air, embedded in the otherwise homogeneous medium mentioned earlier. We find that this approach accurately describes the optical properties of mesoporous TiO₂ films of micrometer thickness. Mie theory (accounting for light diffusion within the porous film) combined with Fresnel equations are implemented in a Monte Carlo formalism with the purpose of describing the trajectory of individual photons illuminating the system and thus the optical properties of the weakly diffusive medium. A genetic algorithm is used to find the configuration of titania and air aggregates that yields the most accurate description of the optical properties of the films among over 10⁶ solutions explored. A wide range of initial conditions yields essentially the same final set of parameters (i.e., air and TiO₂ aggregate size distributions and concentrations), which indicates that the configuration found is a very close representation of the internal nanostructure of the porous materials under study. The same approach can be applied to any optical media characterized by a random dispersion of inclusions in a homogeneous medium regardless of their specific composition (porous and nonporous nanoparticles), shape, and size distribution. It can thus be considered as a noninvasive tool to characterize an arbitrary nanostructure as long as it displays weak scattering properties, provided the total aggregate load is less than 20% in volume.

2. Results and Discussion

A representative scanning electron microscope (SEM) image of a cross section of one of the fabricated TiO₂ porous films is shown in **Figure 1a**. In the image, the porous texture of the 4.8 μm -thick film deposited on a glass substrate is shown. Specifications on

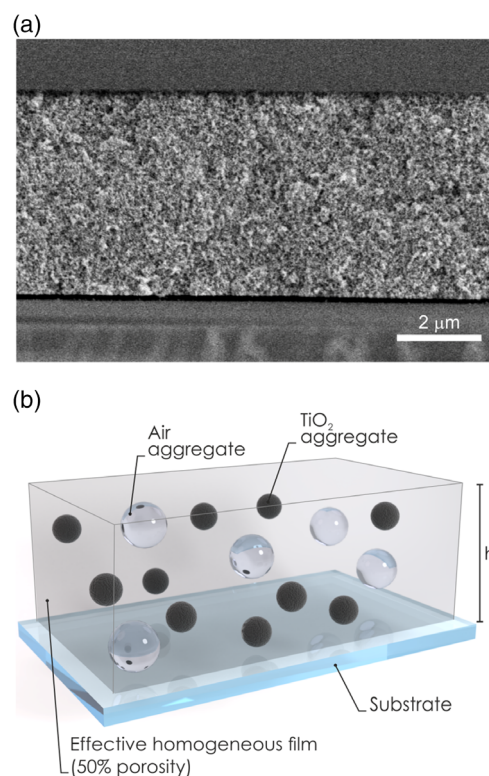


Figure 1. a) SEM image of a cross section of a TiO₂ mesoporous film of 4.8 μm thickness on top of a glass substrate. b) Schematics of the modeled internal nanostructure of the mesoporous TiO₂ film deposited on a glass substrate. It consists of an ensemble of disordered TiO₂ (dark gray) or air (transparent) aggregates of variable size (typically, in the few tens of nanometer range) and total concentration embedded into an extensive semi-transparent nondiffusive homogeneous TiO₂ medium of 50% porosity. The total film thickness is denoted by h .

sample fabrication and optical characterization are provided in Supporting Information. Diffuse scattering from these films is attributed to higher- and lower-spatial variations of the complex refractive index with respect to a background whose optical constants are given by an effective medium approximation. This physical picture accounts for the random formation of regions of higher- (TiO₂) or lower- (air)-density aggregates, distributed inside a nonscattering homogeneous TiO₂ film of 50% porosity, which are responsible for the weakly scattered light observed from these materials. Under these assumptions, the internal nanostructure of the porous film is hereby approximated as two distinct dispersions of disordered spherical nanoparticles of diverse sizes (typically in the few tens of nanometer range) and concentrations made up of TiO₂ and air, embedded in a main nondiffusive TiO₂ film of 50% porosity described as an effective medium whose dielectric constant is given by Bruggeman's equation, which is the most suitable option to describe a system in which pores and solid components are in a similar proportion.^[14] Surface roughness at the air–film interface is accounted for in the model by including a refractive index gradient on the upper side of the structure.^[30] A scheme of the aforementioned internal nanostructure is shown in **Figure 1b**. Please notice that TiO₂ aggregates and air pores

are represented as opaque and transparent spheres respectively, while the main homogeneous TiO₂ background of 50% porosity in which they are contained is represented by a semitransparent rectangular box. The porous film is deposited over a 1 mm-thick glass substrate, and its thickness is denoted by h .

First, scattering and absorption properties of the constituent TiO₂ and air nanospheres forming the internal nanostructure of the porous films are analyzed by means of Mie scattering theory.^[31,32] For Mie calculations, the spectral complex refractive index of the TiO₂ material, along with that of the embedding effective absorbing medium, are needed. Those data are shown in Figure S1, Supporting Information. **Figure 2** shows absorption (Q_{abs}) and scattering (Q_{sc}) cross sections of representative nanosized spherical aggregates made up of either TiO₂ (top left panel) or air (top right) materials, embedded in a TiO₂ film of 50% porosity (whose effective dielectric constant is also computed by means of Bruggeman's model). Angular scattering distributions at selected wavelengths are also displayed (corresponding bottom panels). Larger scattering and absorption cross sections are attained at short wavelengths, decreasing to zero at larger ones. Q_{sc} of TiO₂ aggregates are one order of magnitude higher than those of air pores of equal size and two orders of magnitude larger than the corresponding Q_{abs} (shown in the inset in panel (a)). Notably, small deviations of the particle size (≈ 5 nm) result in large variations of the scattering intensity for both constituent materials. Finally, the scattering angular

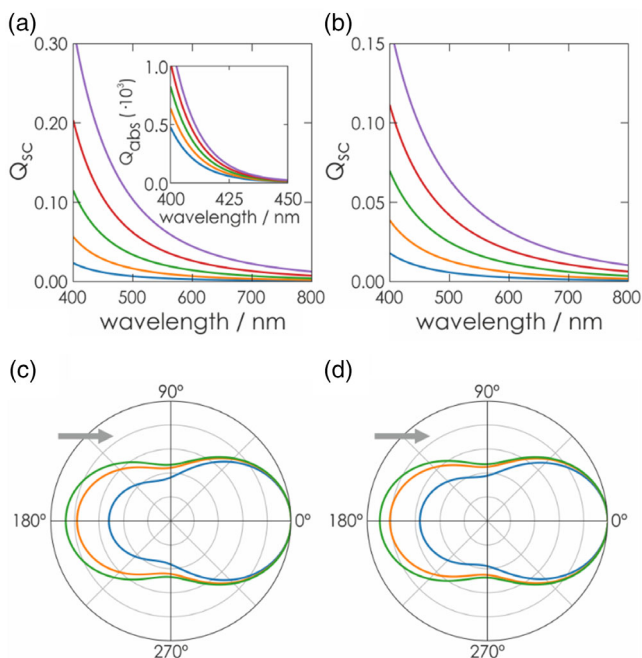


Figure 2. a,b) Scattering cross section (Q_{sc}) of spherical (a) TiO₂ or (b) air aggregates of radius $r = 20$ nm (blue), $r = 25$ nm (orange), $r = 30$ nm (green), $r = 35$ nm (red), and $r = 40$ nm (purple) embedded into a TiO₂ material of 50% porosity (corresponding absorption cross sections (Q_{abs}) are shown as inset). c,d) Angular distribution of scattered light at $\lambda = 400$ nm (blue), $\lambda = 600$ nm (orange), and $\lambda = 800$ nm (green) of (c) TiO₂ spherical aggregates or (d) air nanopores of radius $r = 30$ nm embedded into a TiO₂ material of 50% porosity. The arrows show the incident illumination direction.

distribution is shown in panels (c) and (d) for both materials, displaying high lobes of light directed into the forward (0°) and backward (180°) directions with almost the same probability, as expected when the size of the scatterers is much smaller than the illumination wavelength.

Next, to compute the optical properties of the mesoporous film whose internal nanostructure is described according to the disordered ensemble of TiO₂ and air spherical inclusions depicted in Figure 1b, the same approach applied in other studies^[33–35] is considered. Essentially, all necessary information to evaluate the optical properties of the studied systems relies upon the computation of the trajectory of all photons impinging on the system. Specifically, the system is illuminated from the porous film side. In the model, a Monte Carlo approach is applied and combined with Fresnel equations and a genetic algorithm^[36,37] to calculate the optical characteristics and find the optimal set of parameters, that is, particle size distribution and concentration of both spherical TiO₂ aggregates and air pores, that describe the internal nanostructure of the porous film. Computational details are given in the Supporting Information.

In **Figure 3**, both experimental (a,b) and calculated (c,d) results for the reflectance (in blue) and transmittance (in orange) of two illustrative cases of thin ($h = 4.8 \mu\text{m}$ (a,c)) and thick ($h = 16.3 \mu\text{m}$ (b,d)) porous TiO₂ films are depicted. Specular and ballistic contributions are displayed as solid lines, and diffused light components appear as dashed ones. An excellent agreement between experimental and theoretical results for all light components is attained for the entire set of film thicknesses here considered. Please note that in the case of the thickest film considered ($h = 16.3 \mu\text{m}$ (b,d)), 50% of the incoming light is diffusely scattered at the shortest wavelengths as a result of the presence of small regions of different refractive index herein assumed. Diffused light follows the spectral trend attained for the scattering cross sections calculated by Mie theory in Figure 2, being maximum at short wavelengths and approaching zero at longer ones. Also, as expected, its magnitude increases with film thickness, since the probability of the photon to be deviated from the incident direction is enlarged.

To attain the size and concentration distribution of TiO₂ and air aggregates inside the porous nonscattering film, we used an inverse design using a genetic algorithm. Information about the computational cost is provided in the Supporting Information. Initially, the experimentally measured optical properties (specular, ballistic, and diffused spectral light components, please see Figure 3a,b) of the two films chosen for this analysis were used as input targets to be simultaneously fitted. In the optimization procedure, the following Figure of Merit (FoM) is minimized.

$$\text{FoM} = \sum_{\lambda} \sum_{i=1}^{i=2} [(R_s^T(\lambda, i) - R_s^E(\lambda, i))^2 + (R_d^T(\lambda, i) - R_d^E(\lambda, i))^2 + (T_b^T(\lambda, i) - T_b^E(\lambda, i))^2 + (T_d^T(\lambda, i) - T_d^E(\lambda, i))^2] \quad (1)$$

In the earlier expression, R and T stand for reflectance and transmittance, respectively, subscript s for specular, b for ballistic, and d for diffused light, while superscripts T and E account for theoretical and experimental results, accordingly. Summation over i represents the film considered, being different only in their

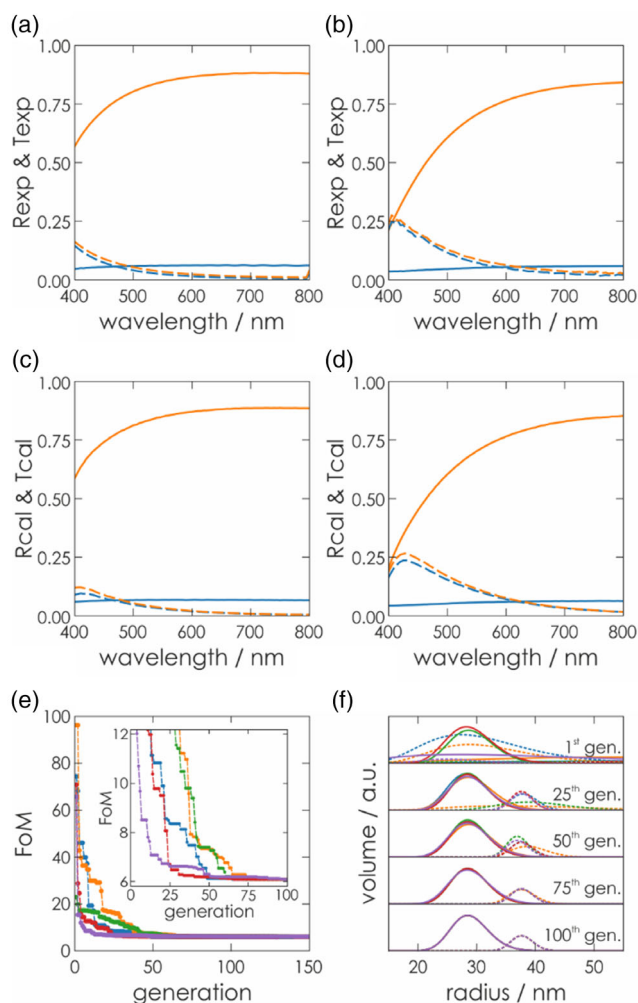


Figure 3. a,b) Experimental specular (diffuse) reflectance in blue solid (dashed) line and ballistic (diffuse) transmittance in orange solid (dashed) line light components of porous TiO₂ films of (a) $h = 4.8 \mu\text{m}$ and (b) $h = 16.3 \mu\text{m}$ thickness. c,d) Calculated light components, following the same color code as in top panels. e) FoM as a function of the generation number, for five diverse initial conditions (corresponding to different colors), which correspond to the evaluation of $\approx 3.5 \times 10^5$ systems. In each curve, only the best solution obtained among the 512 individuals evaluated in each generation is displayed. The inset displays a zoom-in to better appreciate the evolution of the FoM with the generation number. f) For 1, 25, 50, 75, and 100 generations, and different initial conditions (following the same color code as in panel (e)), results show aggregate (i.e., scatterer) size log-normal distribution attained to describe the internal nanostructure of homogeneous TiO₂ films of 50% porosity containing TiO₂ and air aggregates, irrespective of the film thickness. Solid curves correspond to spherical TiO₂ aggregates distributions, while dashed ones to air nanopores.

thickness (4.8 and 16.3 μm). Within the genetic algorithm, 15 different initial families (each made up of 512 individuals) were considered. A total of $\approx 10^6$ systems were evaluated, distributed among ≈ 150 different generations. For each initial condition, the final converged result corresponds to solutions for which the FoM does not change over 50 generations. Data corresponding to those parameters are displayed in Figure S2, Supporting

Information. For simplicity, Figure 3e shows the FoM as a function of the generation number, for five initial conditions (or families) corresponding to different colors in the figure. In each curve, only the best solution obtained among the 512 individuals evaluated in each generation is displayed. As it can be readily seen, all plots converge to the same result after ≈ 100 generations, regardless of the initial conditions. Figure 3f shows, for each set of initial conditions in panel e), and following the same color code, the evolution over different generations (1, 25, 50, 75 and 100) of the log-normal distribution attained for TiO₂ and air aggregates with solid and dashed lines, respectively. Additional results for intermediate thick-film dimensions are shown in Figure S3, Supporting Information. The sizes of both TiO₂ aggregates and air pores are allocated according to a log-normal distribution, such that

$$f(r) = \frac{1}{r\sigma\sqrt{2\pi}} e^{\frac{-(\log(r)-\mu)^2}{2\sigma^2}}$$

For TiO₂ spherical aggregates ($\mu = 3.36$, $\sigma = 0.11$), the most frequent value corresponds to particles of radius $r \approx 28 \text{ nm}$ in a concentration of 2.43%, whereas for air nanopores ($\mu = 3.63$, $\sigma = 0.05$), these values correspond to $r = 38 \text{ nm}$ and a concentration of 0.6%. For the sake of comparison, simulations performed assuming arbitrarily different particle size distributions in a 50% porous film are shown in Figure S4, Supporting Information. They exemplify how different disordered distributions of titania and air aggregates with sizes on the tens of nanometers length scale (i.e., much shorter than the visible wavelengths herein targeted) give rise to very different scattering properties. The fact that the final distributions attained for both TiO₂ spherical aggregates and air pores, which are the ones that best fit the experimental optical data in our model, are independent of the initial conditions allows us to consider them as accurate representations of the actual internal nanostructure of the porous film.

Finally, the angular distribution of the diffused light in both transmission and reflection regions is also computed. In Figure 4, we analyze the scattered light distribution of a $h = 4.8 \mu\text{m}$ film (left panels) and a $h = 16.3 \mu\text{m}$ film (right panels) at $\lambda = 400 \text{ nm}$ (in blue) and $\lambda = 600 \text{ nm}$ (in orange), which correspond to two different representative scattering scenarios. Details of the calculations are provided in the Supporting Information, and a scheme of the employed theoretical angular distribution detection is shown in Figure S5, Supporting Information. In Figure 4a–d, light scattered into the transmission region corresponds to the angular range $90^\circ > \varphi > 270^\circ$, whereas light scattered back to the reflection region enter within the angular range $90^\circ < \varphi < 270^\circ$. In both cases, the incident illumination direction corresponds to $\varphi = 180^\circ$. In order to appreciate the angular distribution characteristics, only scattered photons are considered in the figure, and ballistic and specular photons are excluded. Results in Figure 4a,b show an almost symmetric light-scattered distribution displaying high lobes of directed light into the transmission and reflection regions, consistent with the Mie scattering distribution of single TiO₂ aggregates or air pores in Figure 2. Medium panels show a zoom-in of the panels on top to show a finer view of the scattering features and their dependence with the incident wavelength. At $\lambda = 600 \text{ nm}$ (in orange), less light is scattered (in agreement with reflectance and transmittance results), and the symmetric light

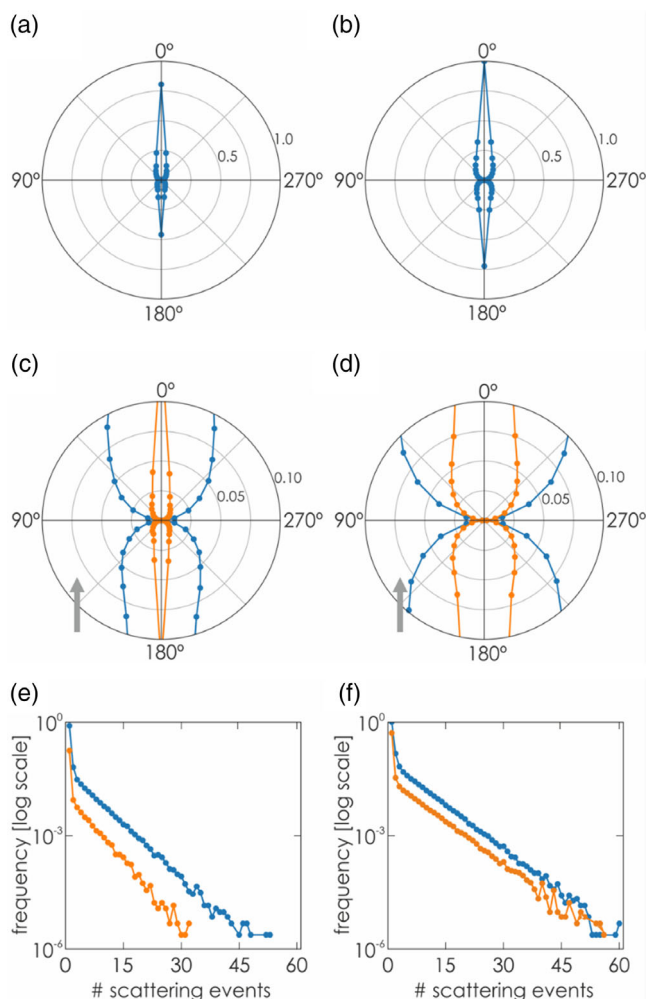


Figure 4. a–d) Angular distribution of just scattered light scattered off-normal (excluding ballistic and specular photons) in TiO_2 films of thickness $h = 4.8 \mu\text{m}$ (left panels) and $h = 16.3 \mu\text{m}$ (right panels) at $\lambda = 400 \text{ nm}$ (blue) and $\lambda = 600 \text{ nm}$ (orange). Incident light comes from $\varphi = 180^\circ$ (as indicated by the gray arrow), transmitted light scattered corresponds to the angular range $90^\circ > \varphi > 270^\circ$, and reflected light scattered to $90^\circ < \varphi < 270^\circ$; the arrows show the incident illumination. (a,b) Zoom-out and (c,d) zoom-in of the same results revealing specific angular distribution features. e–f) Corresponding scattering event histograms in logarithmic scale following the same color code of the panels on top.

distribution narrows with respect to the $\lambda = 400 \text{ nm}$ case (in blue). Bottom panels display, in logarithmic scale and for each illumination wavelength following the same color code as in panels on top, a histogram of the scattered events. Interestingly, in all cases, most of the photons that escape from the system undergo only one scattering event. In the case of thin films, all photons will exit the system after ≈ 45 scattering events at $\lambda = 400 \text{ nm}$, and this number reduces to ≈ 35 at $\lambda = 600 \text{ nm}$. For thick films, the maximum number of scattering events will be ≈ 60 and ≈ 55 , at $\lambda = 400 \text{ nm}$ and $\lambda = 600 \text{ nm}$, respectively. Please note that this information can exclusively be accessed through a theoretical model.

3. Conclusion

In conclusion, we have presented a theoretical model that accounts for the optical properties of weakly scattering media on the grounds of a physically meaningful description of nanoporous films. An ensemble of disordered dispersions of air nanopores and dense aggregates in an optically homogeneous nondiffusive background is considered. Results of the model are successfully compared to experimental measurements attained from films made of packing of TiO_2 nanocrystals. Results allow not only distinguishing among diffused, ballistic, and specular components, but also elucidating the angular distribution of the scattered light. By combining the Fresnel equations with scattering Mie theory and making use of a genetic algorithm implemented in a Monte Carlo approach, the theoretical approach used provides the most probable solution of the set of parameters (aggregate size distribution and concentration) that describe the internal nanostructure of the porous film. We demonstrate that such a set of parameters is applicable to describe the experimental optical properties of all films with a similar nanostructure, regardless of their thickness. The concept described in this work is generic and can be applied to other low-diffusive porous materials, not only to describe their optical properties but also to resolve their internal nanostructure.

Supporting Information

Supporting Information is available from the Wiley Online Library or from the author.

Acknowledgements

Financial support of the Spanish Ministry of Science and Innovation under grant PID2020-116593RB-I00, funded by MCIN/AEI/10.13039/501100011033, and of the Junta de Andalucía under grant P18-RT-2291 (FEDER/UE), is gratefully acknowledged. A.J.-S. gratefully acknowledges Spanish Ministry of Universities for funding through a Beatriz Galindo Research fellowship BG20/00015.

Conflict of Interest

The authors declare no conflict of interest.

Data Availability Statement

The data that support the findings of this study are available at Digital CSIC at <https://doi.org/10.20350/digitalCSIC/15108>. A simplified version of the code employed for calculating the effect of the weak optical disorder on the scattering may be found at <https://github.com/Multifunctional-Optical-Materials-Group>.

Keywords

diffuse light, optical disorders, porous materials, theoretical modeling, TiO_2 , weakly scattering media

Received: September 21, 2022

Revised: January 17, 2023

Published online: March 19, 2023

- [1] J. Bertolotti, O. Katz, *Nat. Physics*, **2022**, 18, 1008.
- [2] G. I. Marchuk, G. A. Mikhailov, M. A. Nazareliev, R. A. Darbinjan, B. A. Kargin, B. S. Elepov, *The Monte Carlo Methods in Atmospheric Optics*, Vol. 12, Springer, Berlin **2013**.
- [3] V. Tuchin, *J. Biomed. Photonics Eng.* **2015**, 1, 98.
- [4] V. Hwang, A. B. Stephenson, S. Barkley, S. Brandt, M. Xiao, J. Aizenberg, V. N. Manoharan, *Proc. Natl. Acad. Sci.*, **2022**, 118, 2015551118.
- [5] M. Rothhammer, C. Zollfrank, K. Busch, G. von Freymann, *Adv. Opt. Mater.*, **2021**, 9, 2100787.
- [6] B. T. Draine, B. S. Hensley, *Astrophys. J.* **2021**, 910 47.
- [7] O. Lib, Y. Bromberg, *Nat. Phys.* **2022**, 18, 986.
- [8] K. Vynck, R. Pierrat, R. Carminati, L. S. Froufe-Pérez, F. Scheffold, R. Sapienza, S. Vignolini, J. J. Sáenz, arXiv:2106.13892v1.
- [9] S. A. Prahl, M. J. C. van Gemert, A. J. Welch, *Appl. Opt.* **1993**, 32, 559.
- [10] M. E. Davis, *Nature* **2002**, 417, 813.
- [11] J. H. Swisher, L. Jibril, S. H. Petrosko, C. A. Mirkin, *Nat. Rev. Mater.* **2022**, 7, 428.
- [12] A. Rubino, L. Calì, A. García-Bennett, M. E. Calvo, H. Míguez, *Adv. Opt. Mater.* **2020**, 8, 1901868.
- [13] M. Grätzel, *J. Photochem. Photobiol. C* **2003**, 4, 145.
- [14] B. O'Regan, M. Grätzel, *Nature* **1991**, 353, 737.
- [15] S. Rashidi, J. A. Esfahani, N. Karimi, *Renewable Sustainable Energy Rev.* **2018**, 91, 229.
- [16] A. Corma, *Chem. Rev.* **1997**, 97, 2373.
- [17] E. J. Anglin, L. Cheng, W. R. Freeman, M. J. Sailor, *Adv. Drug. Delivery Rev.* **2008**, 60, 1266.
- [18] N. Obata, Y. Mikami, H. Yoshioka, Y. Oki, *Adv. Photonics Res.* **2022**, 3, 2200018.
- [19] M. Rothhammer, C. Zollfrank, K. Busch, G. von Freymann, *Adv. Opt. Mater.* **2021**, 9, 2100787.
- [20] B. Yuan, X. Zhang, J. Yu, L. Zhou, B. Luo, Y. Liu, R. Chen, *Adv. Mater. Interfaces* **2022**, 9, 2201366.
- [21] J. C. A. D'auriac, P. E. Wolf, *Phys. Rev. E* **2022**, 105, 064106.
- [22] V. Estes, S. Carretero-Palacios, H. Míguez, *J. Phys. Chem. Lett.* **2022**, 13, 4513.
- [23] N. Hidalgo, C. López-López, G. Lozano, M. E. Calvo, H. Míguez, *Langmuir* **2012**, 28, 13777.
- [24] D. A. Bruggeman, *Ann. Phys.* **1935**, 416, 636.
- [25] J. C. Maxwell Garnet, *Philos. Trans. R. Soc. A* **1904**, 203, 359.
- [26] P. Yeh, *Optical Waves in Layered Media*, Wiley, New York, NY, USA, **2008**.
- [27] A. Yella, S. Mathew, S. Aghazada, P. Comte, M. Grätzel, M. K. Nazeeruddin, *J. Mater. Chem. C*, **2017**, 5, 2833.
- [28] A. Fujishima, T. N. Rao, D. A. Tryk, *J. Photochem. Photobiol. C* **2000**, 1, 1.
- [29] G. K. Mor, O. K. Varghese, M. Paulose, K. Shankar, C. A. Grimes, *Sol. Energy Mater. Sol. Cells*, **2011**, 206, 90.
- [30] P. Löper, M. Stuckelberger, B. Niesen, J. Werner, M. Filipič, S.-J. Moon, J.-H. Yum, M. Topič, S. De Wolf, C. Ballif, *J. Phys. Chem. Lett.*, **2015**, 6, 66.
- [31] C. F. Bohren, D. R. Huffman, *Absorption and Scattering of Light By Small Particles*, Wiley, New York, NY, **1983**.
- [32] I. Wayan Sudiarta, P. Chylek, *J. Opt. Soc. Am. A* **2001**, 18, 1275.
- [33] F. E. Gálvez, P. R. F. Barnes, J. Halme, H. Míguez, *Energy Environ. Sci.* **2014**, 7, 689.
- [34] J. M. Miranda-Muñoz, S. Carretero-Palacios, A. Jiménez-Solano, Y. Li, G. Lozano, H. Míguez, *J. Mater. Chem. A* **2016**, 4, 1953.
- [35] Y. Li, S. Carretero-Palacios, K. Yoo, J. H. Kim, A. Jiménez-Solano, C.-H. Lee, H. Míguez, M. J. Ko, *Energy Environ. Sci.* **2016**, 9, 2061.
- [36] A. Jiménez-Solano, M. Anaya, M. E. Calvo, M. Alcon-Camas, C. Alcañiz, E. Guillén, N. Martínez, M. Gallas, T. Preussner, R. Escobar-Galindo, H. Míguez, *Adv. Opt. Mater.* **2017**, 5, 1600833.
- [37] D. E. Goldberg, *Genetic Algorithms in Search, Optimization and Machine Learning*, Addison-Wesley, Boston, MA **1989**.